



HAL
open science

Complex 3-D Surface Deformation in the 1971 San Fernando, California Earthquake Reveals Static and Dynamic Controls on Off-Fault Deformation

É. Gaudreau, James Hollingsworth, E. Nissen, G J Funning

► **To cite this version:**

É. Gaudreau, James Hollingsworth, E. Nissen, G J Funning. Complex 3-D Surface Deformation in the 1971 San Fernando, California Earthquake Reveals Static and Dynamic Controls on Off-Fault Deformation. *Journal of Geophysical Research: Solid Earth*, 2023, 128 (3), 10.1029/2022JB024985 . hal-04309168

HAL Id: hal-04309168

<https://hal.science/hal-04309168v1>

Submitted on 27 Nov 2023

HAL is a multi-disciplinary open access archive for the deposit and dissemination of scientific research documents, whether they are published or not. The documents may come from teaching and research institutions in France or abroad, or from public or private research centers.

L'archive ouverte pluridisciplinaire **HAL**, est destinée au dépôt et à la diffusion de documents scientifiques de niveau recherche, publiés ou non, émanant des établissements d'enseignement et de recherche français ou étrangers, des laboratoires publics ou privés.

JGR Solid Earth

RESEARCH ARTICLE

10.1029/2022JB024985

Key Points:

- Correlation of aerial photographs reveals significant left-lateral surface deformation in the 1971 San Fernando earthquake
- Off-fault deformation is partitioned between the fault trace-parallel and vertical components of deformation
- Primary controls of off-fault deformation may be different for the fault trace-parallel and vertical components

Supporting Information:

Supporting Information may be found in the online version of this article.

Correspondence to:

É. Gaudreau,
gaudreau@uvic.ca

Citation:

Gaudreau, É., Hollingsworth, J., Nissen, E., & Funning, G. J. (2023). Complex 3-D surface deformation in the 1971 San Fernando, California earthquake reveals static and dynamic controls on off-fault deformation. *Journal of Geophysical Research: Solid Earth*, 128, e2022JB024985. <https://doi.org/10.1029/2022JB024985>

Received 17 JUN 2022

Accepted 27 FEB 2023

Author Contributions:

Conceptualization: É. Gaudreau
Data curation: É. Gaudreau
Formal analysis: É. Gaudreau
Funding acquisition: É. Gaudreau, J. Hollingsworth, E. Nissen, G. J. Funning
Methodology: J. Hollingsworth
Software: J. Hollingsworth
Supervision: J. Hollingsworth, E. Nissen
Visualization: É. Gaudreau
Writing – original draft: É. Gaudreau
Writing – review & editing: É. Gaudreau, J. Hollingsworth, E. Nissen, G. J. Funning

© 2023 The Authors.

This is an open access article under the terms of the [Creative Commons Attribution-NonCommercial License](#), which permits use, distribution and reproduction in any medium, provided the original work is properly cited and is not used for commercial purposes.

Complex 3-D Surface Deformation in the 1971 San Fernando, California Earthquake Reveals Static and Dynamic Controls on Off-Fault Deformation

É. Gaudreau¹ , J. Hollingsworth² , E. Nissen¹ , and G. J. Funning³ 

¹University of Victoria, Victoria, BC, Canada, ²Université Grenoble Alpes, Université Savoie Mont Blanc, CNRS, IRD, Université Gustave Eiffel, Grenoble, France, ³University of California Riverside, Riverside, CA, USA

Abstract The shallow 1971 M_w 6.6 San Fernando, California earthquake involved a complex rupture process on an immature thrust fault with a non-planar geometry, and is notable for having a higher component of left-lateral surface slip than expected from seismic source models. We extract its 3-D coseismic surface displacement field from aerial stereo photographs and document the amount and width of the vertical and fault trace-parallel components of distributed deformation along strike. The results confirm the significant left-lateral surface offsets, suggesting a slip vector rotation at shallow depths. Comparing our offsets against field measurements of fault slip, we observe that most of the offset was accommodated in the damage zone, with off-fault deformation averaging 69% in both the fault trace-parallel and vertical components. However, the magnitude and width of off-fault deformation behave differently between the vertical and fault trace-parallel components, which, along with the rotation in rake near the surface, can be explained by dynamic rupture effects.

Plain Language Summary The 1971 San Fernando, California earthquake is infamous for its strong ground motions and large lateral fault offsets measured in the field, despite the compressional tectonic stresses that triggered the earthquake. We produce maps of the 3-D surface deformation that occurred during the earthquake by comparing pre-earthquake and post-earthquake aerial photographs of this area. The results confirm the presence of important lateral and compression-driven deformation at the surface. This surface deformation was distributed over a wide zone, and as such, previously reported field measurements did not capture the total slip that occurred at the surface. Understanding controls on the width of the deformation zone provides insight into earthquake behavior and helps improve our estimates of seismic hazard. Our results show that during the San Fernando earthquake, lateral and compression-driven deformation behaved differently within the fault zone, which may suggest that the two slip components were affected by different factors and damage generation mechanisms.

1. Introduction

As a fault zone accumulates damage during many earthquake cycles, its geometrical and material properties change, which may in turn play a significant role in earthquake rupture behavior (e.g., Bürgmann et al., 1994; Manighetti et al., 2007; Perrin et al., 2016; Thakur & Huang, 2021; Wesnousky, 1990). Although there is no single metric for the maturity of a fault due to the many factors that affect fault evolution (e.g., cumulative slip, varying fault healing rates), faults are generally considered immature if they have not hosted many earthquakes and as a result have not yet developed an efficient system for localizing deformation (Ben-Zion & Sammis, 2003; Dolan & Haravitch, 2014). A fault zone's elastic moduli weaken as it matures, resulting in a zone of low seismic velocities in which deformation becomes progressively more localized (e.g., Cochran et al., 2009; Dolan & Haravitch, 2014). As faults accrue more slip, fault traces become straighter, and separate fault segments coalesce (Manighetti et al., 2007, 2021; Wesnousky, 1988, 1990). Fault step-overs and other geometric complexities may limit earthquake rupture propagation, and thus earthquakes are perhaps more likely to rupture over a larger area on mature faults than on immature faults (Huang, 2018; Manighetti et al., 2007; Wesnousky, 1988, 1990). The segmentation and roughness of immature faults produce heterogeneities in stress and fault strength and may be an important factor in triggering supershear rupture velocities (Bruhat et al., 2016). However, smoother, more mature fault segments are otherwise more likely to sustain fast rupture velocities, while immature faults are typically associated with slower rupture velocities and a more irregular slip distribution (Bruhat et al., 2016, 2020;

Bürgmann et al., 1994; Perrin et al., 2016; Pousse-Beltran et al., 2020). The progressive development of the damage zone and simplification of the fault geometry is associated with lower stress drops, more regular recurrence intervals, and influences hypocenter depths (Berryman et al., 2012; Harrington & Brodsky, 2009; Radiguet et al., 2009; Thakur et al., 2020; Thakur & Huang, 2021; Wesnousky, 1990; Zielke et al., 2017). The complexity of the fault geometry also seems to be an important factor controlling the delocalization of seismic slip (Antoine et al., 2021; Dolan & Haravitch, 2014; Milliner et al., 2015). Since immature faults are associated with deformation distributed tens of meters to kilometers beyond the main slip surfaces, primary fault offsets observed in the field in the fault core fall short of the total coseismic offset, which may result in an underestimation of the fault slip rate and seismic hazard (e.g., Cheng & Barnhart, 2021; Milliner et al., 2015). Furthermore, geodetic modeling that simplifies the fault zone to a planar feature in a purely elastic medium often overlooks near-surface displacements and inelastic deformation (e.g., Cheng & Barnhart, 2021; Dolan & Haravitch, 2014; Milliner et al., 2021). Studying the behavior of immature faults is important for seismic hazard assessments as the hazard around these faults is often underestimated until a strong and potentially damaging earthquake occurs (e.g., Gaudreau et al., 2019; Jackson et al., 2006; Quigley et al., 2012).

In this study, we use the term “off-fault deformation” (OFD) to refer to the deformation that occurs in the wide (tens of meters to kilometers) zone of damaged rock around the high-strain fault core. This includes deformation accommodated by micro- and macrofracturing, warping, granular flow, and block rotation, and consists of both elastic and inelastic deformation (e.g., Cheng & Barnhart, 2021; Milliner et al., 2015; Scott et al., 2018). Distributed deformation in the shallow crust is thought to be one of the factors causing apparent shallow slip deficits, the systematic reduction in shallow crustal slip compared to greater slip at depth based on geodetic elastic dislocation models (e.g., Fialko et al., 2005; Kaneko & Fialko, 2011; Xu et al., 2016). Different mechanisms contribute toward OFD generation during an earthquake, such as the formation of a cloud of microcracks around the rupture tip as it propagates (Lockner et al., 1991; Lyakhovskiy et al., 1997; Martel et al., 1988), seismic waves propagating ahead of the rupture front (Jara et al., 2021; Ma, 2008; Thomas & Bhat, 2018) and the zone of high strain rate around the dynamically-propagating rupture front (Andrews, 1976; Poliakov et al., 2002; Rice et al., 2005). Moreover, stress heterogeneities caused by continued slip on a rough fault surface after the passage of the rupture front generate additional off-fault damage (Chester & Chester, 2000; Dieterich & Smith, 2009).

We assess the role of structural complexity, fault maturity and near-surface geological material on the distribution of OFD. Straighter, structurally simpler and more mature fault segments, as well as stronger near-surface materials tend to promote more uniform slip and localized deformation, and thick, undeformed sediments and partially indurated sedimentary rocks are thought to delocalize deformation (Dolan & Haravitch, 2014; Milliner et al., 2015; Roten et al., 2017; Zinke et al., 2014). Other factors commonly affecting OFD distribution include damage inherited from previous earthquakes (e.g., Cochran et al., 2009; Fialko et al., 2002; Zinke et al., 2014). Most of the aforementioned studies focus on strike-slip earthquakes, and OFD in thrust earthquakes is relatively poorly studied, in part because surface-rupturing thrust earthquakes are relatively uncommon. The oblique 1971 San Fernando, California earthquake is a well-known case study of a destructive rupture on a thrust fault that was poorly studied prior to the earthquake and featured strong ground motions (Wentworth et al., 1971). The San Fernando Fault is immature based on several factors including its relatively low slip rate of 2–3 mm/year, its relatively short 16 km fault length within the ~140-km-long Sierra Madre Fault System, and its relatively high density of step-overs with widths >1% of the fault length (~3 wide step-overs within 16 km; Burgette et al., 2020; Lindvall & Rubin, 2008; Manighetti et al., 2007; Manighetti et al., 2021; Wells & Coppersmith, 1994). Here, we extract the complex 3-D coseismic deformation field from high-resolution stereo aerial photographs, and assess the factors controlling the width and amount of distributed deformation in an earthquake with a significant thrust component. Offsets and OFD magnitude and width are measured by profiling the displacement field at regular intervals along strike. Their distribution along with changes in fault geometry and geology allow us to explore which factors may control the surface expression of near-fault coseismic deformation. Notably, spatial patterns of OFD magnitude and deformation zone widths are different in the fault trace-parallel and vertical components, which may reflect the complexity of the rupture and the combination of static and dynamic processes affecting the distribution of deformation.

2. Tectonic Setting and Fault Structure

The WNW-striking, north-dipping San Fernando Fault is located in the Transverse Ranges of California, USA, in the transpressional region south of the San Andreas Fault’s “big bend” (Figure 1). The Transverse Ranges are

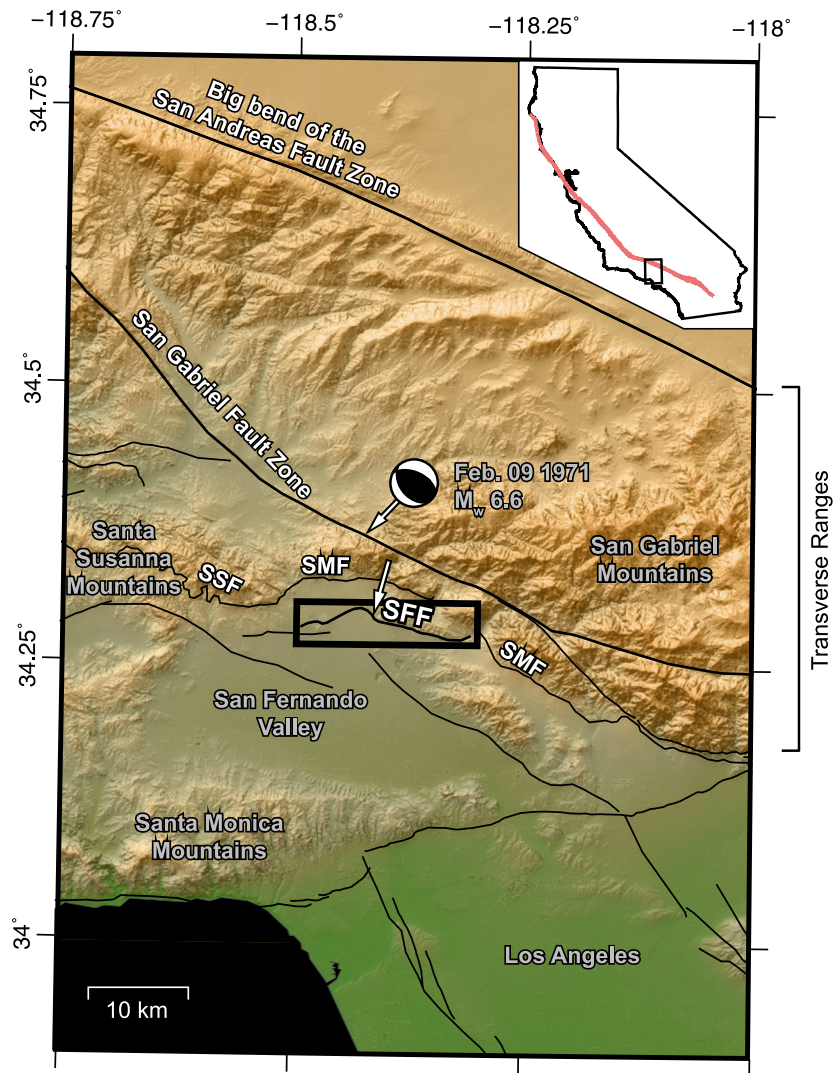


Figure 1. Active fault map around the San Fernando area. Thin black lines are surface fault traces from the U.S. Geological Survey Quaternary Fault and Fold Database (<https://doi.org/10.5066/F7S75FJM>) and Whitcomb et al. (1973) determined the focal mechanism from P-wave first motions. White arrows show slip vector azimuths for the deeper and shallower portions of the rupture based on local and teleseismic waveform modeling (Heaton, 1982). Rectangle shows location of Figure 2A. SSF: Santa Susana Fault; SMF: Sierra Madre Fault; SFF: San Fernando Fault. Inset shows the location of the main figure (black rectangle) and San Andreas Fault (red line) within the state of California.

characterized by substantial late Cenozoic north-south shortening and numerous east-west strike-slip and thrust faults (Wentworth et al., 1971). The surface ruptures from the 1971 earthquake are situated in the San Fernando Valley of the Greater Los Angeles area, which is bounded to the north by the Santa Susana and San Gabriel Mountains, and to the south by the Santa Monica Mountains. The compressional axis of the regional stress field is oriented N-S to NNE-SSW (e.g., Stein et al., 1994). The San Gabriel Mountains are the result of 5–10 million years of thrusting on structures such as the Sierra Madre and Santa Susana Faults (Figure 1). Despite the presence of many young faults in the San Gabriel Mountains, the San Fernando area was characterized by scarce seismicity prior to the 1971 earthquake (Wentworth et al., 1971), with fewer than 10 earthquakes larger than magnitude 4.0 recorded in and around the San Fernando Valley (USGS COMCAT catalog; <https://earthquake.usgs.gov/earthquakes/search/>). Before 1971, the most notable event in the region is the historical Pico Canyon earthquake of 1893, for which there were reports of strong shaking and multiple landslides (Townley & Allen, 1939). As a result, the San Fernando Fault and many others in the San Gabriel Mountains were either unknown or not widely considered to be active at the time (Wentworth et al., 1971; Weber, 1975, and references therein).

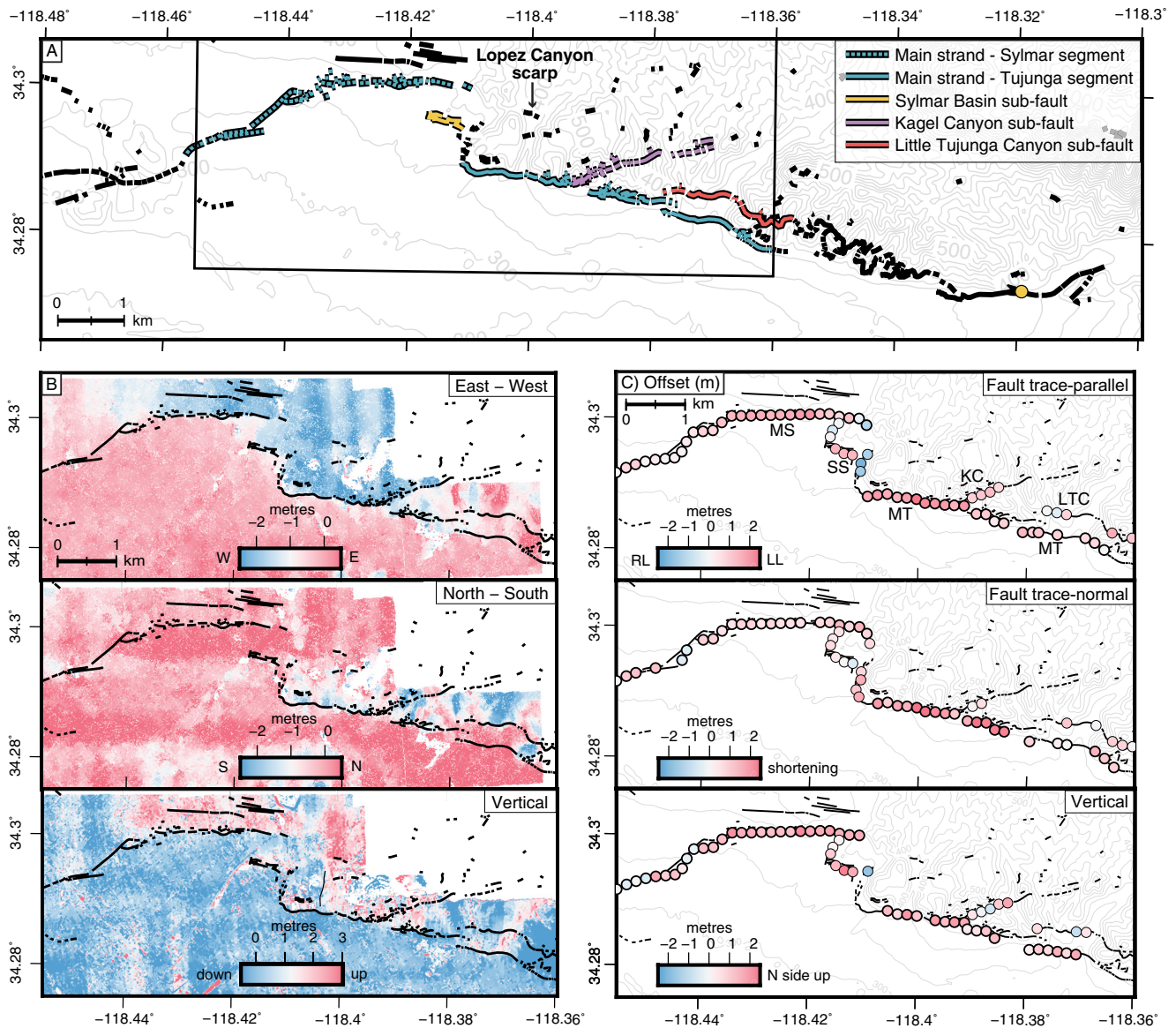


Figure 2. (a) Surface rupture of the 1971 San Fernando earthquake (USGS Quaternary fault and fold database of the United States; <https://www.usgs.gov/programs/earthquake-hazards/faults>; Bonilla et al., 1971; Wentworth et al., 1971; Proctor et al., 1972; Kahle, 1975). Rectangle corresponds to the area analyzed using aerial photographs. Gray contour lines show the topography in meters: the Sylmar segment in the west cuts through the San Fernando basin, while the Tujunga segment intersects the surface at the foothills of the San Gabriel Mountains. Yellow circle: location in Kahle (1975) where curved slickenlines recorded initial left-lateral slip then thrust-oriented slip. Curved slickenlines were also found by Bonilla et al. (1971) at the Lopez Canyon scarp although no interpretation was reported. (b) Coseismic displacement field of the 1971 San Fernando earthquake from optical image correlation and DEM differencing. Thin north-south-oriented line in the vertical panel traces the zone of vertical offset mapped by Barrows et al. (1975) (see Section 4.1). (c) Offset measurements from fault trace-perpendicular displacement profiles. Circles with thick outlines correspond to measurements on main fault strands used for averages in Sections 4 and 5.

The 1971 surface rupture consists of two north-dipping main segments offset by a 1.3 km right step: the west-striking Sylmar segment cross-cutting the San Fernando Valley, and to the east, the WNW-striking Tujunga segment, a valley-bounding fault south of the San Gabriel Mountains (Figure 2a; Wentworth et al., 1971). Secondary surface ruptures identified after the earthquake include the Sylmar Basin secondary fault in the footwall which is sub-parallel to the main strand's Sylmar segment, and the Kagel Canyon secondary fault that cuts across the San Gabriel Mountains at a 30° angle from the main Tujunga segment. Farther east is the Little Tujunga Canyon secondary fault, sub-parallel to the main fault (Figure 2a). These fault segments are thought to represent an increase in fault complexity near the surface (e.g., Carena & Suppe, 2002; Savage et al., 1975). At depth, the San Fernando Fault cuts through dense, crystalline basement (Langenheim et al., 2011; Tsutsumi & Yeats, 1999;

Wentworth et al., 1971). Near the surface, the Sylmar segment cuts through ~4–5 km of sedimentary rocks, including moderately indurated Late Miocene and Early Pliocene sandy siltstone, sandstone and shale overlain by undeformed and partially indurated Pleistocene conglomerate, and alluvium (Langenheim et al., 2011; Wentworth et al., 1971). The Tujunga segment cuts through crystalline basement and ~1–1.5 km of the Late Miocene siltstone and sandstone formation (Langenheim et al., 2011). Field and seismic reflection data have suggested that the fault follow bedding planes near the surface, with the Sylmar segment dipping 55°–60° and the Tujunga segment ~25° (Barrows, 1975; Kamb et al., 1971; Sharp, 1975; Tsutsumi & Yeats, 1999; Weber, 1975).

The Sylmar segment coincides with a >8-m-high pre-existing fault scarp, but paleoseismic offset could not be determined (Heath & Leighton, 1973; Weber, 1975). In the Tujunga segment, paleoseismic trenches uncovered slip surfaces indicative of prior faulting including >3.5 m of reverse slip in one location, and in another, >13 m of Late Miocene sedimentary rocks overlying undated alluvium and highly deformed hanging wall rocks near the slip surface (Barrows, 1975; Heath & Leighton, 1973). Further, a trench that was excavated across the Lopez Canyon secondary fault (see Figure 2a) showed evidence of ~1 m of slip prior to the San Fernando earthquake, which occurred between 100 and 300 years ago and is thought to have involved rupture of the entire San Fernando fault system (Bonilla, 1973). While there is a scarcity of information on the slip history of the San Fernando Fault, the greater density of macroscopic undulations in the Sylmar segment compared to the Tujunga segment may imply that the Tujunga segment is more mature (Figure 2a; Manighetti et al., 2021).

The 1971 San Fernando earthquake ruptured one of multiple splays off a north-dipping decollement that continues further south (Fuis et al., 2003). The focal mechanism in Figure 1 was determined by Whitcomb et al. (1973) using P-wave first motions, and thus only represents the initial slip. It is generally agreed upon that the down-dip structure must be more complex than a single fault plane (e.g., Whitcomb et al., 1973), as the surface projections of such models are not consistent with the location of the observed surface rupture trace. Furthermore, teleseismic waveform modeling studies have demonstrated the complexity of the rupture with moment tensor solutions that have high CLVD components for a single point source (Barker & Langston, 1982; Kim, 1989). Multiple studies propose an evolving seismic source where the deeper slip has an oblique rake of 76°–84° and the slip shallower than ~5–8 km has a rake of 89° or 90° (Figure 1; Heaton & HelMBERGER, 1979; Heaton, 1982; Kim, 1989; Langston, 1978). These models include either (A) a fault where the dip changes with depth (e.g., Carena & Suppe, 2002; Heaton & HelMBERGER, 1979; Langston, 1978), or (B) two subparallel faults, one surface rupturing and the other a deeper and buried rupture (Heaton, 1982; Kim, 1989). Aftershock relocations form a plane that dips ~40° (Mori et al., 1995) and nodal planes from moment tensor solutions of the deeper segments dip between 29° and 54° (Heaton, 1982; Kim, 1989; Langston, 1978).

Contrary to the seismic data indicating that the bulk of the slip style was thrust, field data and horizontal control geodetic surveys collected in the 1960s and 1970s indicate left-lateral coseismic surface offsets that are roughly equivalent in amplitude to the vertical offsets, reaching ~1.9 m on the Sylmar segment (e.g., Barrows et al., 1973; Bonilla et al., 1971; Kamb et al., 1971; Meade & Miller, 1973; Savage et al., 1975). The surface rupture traces were discontinuous but well-defined, although fault surface exposures were rare and thus most slip measurements were made using offset surface features and visual projection of scarp heights (e.g., Bonilla et al., 1971; Kamb et al., 1971; Sharp, 1975). Field teams noted much more slip variability over short distances along the Tujunga segment than the Sylmar segment. Offset measurement challenges included landsliding, roadwork, lack of exposure because of vegetation and buildings, and streets and sidewalks accommodating deformation differently than the underlying geology (Barrows, 1975; Bonilla et al., 1971; Kamb et al., 1971; Sharp, 1975). These difficulties further motivate the application of novel remote sensing techniques to better characterize the surface deformation.

3. Methods

3.1. Digital Elevation Model Generation and Image Orthorectification

We obtained high-resolution scans of historical stereo aerial photographs of the study area acquired in 1969 and 1972 from the United States Geological Survey's Center for Earth Resources Observation and Science (EROS; <http://earthexplorer.usgs.gov>). Image identifiers and acquisition dates are listed in Table S1 in Supporting Information S1. The scope of the pre-earthquake aerial survey was to image the San Fernando Valley, therefore providing limited coverage of the hanging wall: other pre-earthquake datasets that had broader coverage suffered greatly in terms of striping artifacts and other sources of noise. We reduced errors created by scanning by first

rotating and cropping the photographs such that the corner fiducials were located at the corners of the scan. We enhanced the image contrast using contrast-limited adaptive histogram equalization, and applied a Gaussian blur ($\sigma = 0.5$) to reduce speckle.

To orthorectify the photographs, we produced pre-earthquake and post-earthquake DEMs using the open-source photogrammetry software Ames Stereo Pipeline (ASP), which has extensive documentation and applications in digital Earth observation datasets, historical (scanned film) datasets as well as Lunar and Martian images (Beyer et al., 2018). Orthorectification accuracy depends on the accuracy of the area of interest's topography, the position and orientation of the camera, as well as the camera's intrinsic parameters including focal length, principal point and distortion coefficients. Since historical imagery usually has very limited metadata, the ASP workflow for processing historical imagery begins by computing estimates for each camera's extrinsic parameters. This is done using the THEIA Structure from Motion library (<http://www.theia-sfm.org/index.html>) invoked from ASP, given initial intrinsic parameter values which are fixed in this step (in this study, the U.S. Geological Survey [USGS] provided the initial estimates for focal lengths, and we assumed the optical center to be in the center of the cropped and rotated image). We then use ASP to perform a bundle adjustment with ground control points collected using SRTM as a reference DEM to estimate absolute camera positions (Ajlou et al., 2021).

We further refine the intrinsic and extrinsic parameters of each camera by collecting dense and uniformly distributed match points between overlapping images, and using these in subsequent bundle adjustments where intrinsic and extrinsic parameters for multiple cameras in the dataset are jointly optimized. The stereo reconstruction (i.e., DEM-creation) process is performed using images that are projected onto a reference DEM, and ASP's MGM Final stereo matching algorithm. Normally the reference DEM has a much coarser resolution than the aerial photographs, which supplies the stereo reconstruction with the long-wavelength topography of the area of interest; however, due to the highly varied topography of the study region, we use a 1-m lidar DEM (USGS 3D Elevation Program; <https://www.usgs.gov/core-science-systems/ngp/3dep>) since lower resolution reference DEMs lead to great inaccuracies in the stereo reconstruction. The use of a high-resolution reference DEM may add to the high-frequency noise of the DEMs generated. The resulting point clouds may be shifted in space from the reference DEM, and therefore are then aligned to the reference DEM using an iterative closest point algorithm (using the libpointmatcher library, invoked from ASP; <https://github.com/ethz-asl/libpointmatcher>). We obtained optimal results when we aligned the point clouds from each stereo pair independently to the reference DEM, and a subsequent bundle adjustment jointly optimized the camera parameters for all cameras. Bundle adjustments are most successful in jointly optimizing multiple cameras when there is large (e.g., 60%) overlap between adjacent photographs. However, a joint optimization may be performed over multiple flight lines by collecting interest points in the side lap. This optimization may suffer due to errors introduced by the large perpendicular baseline between flight lines resulting in greater stereoscopic differences, and by illumination differences due to the passage of time between flight lines. Moreover, the overlap area is small (e.g., <30%), and scanning artifacts introduce additional errors (the latter also affect bundle adjustments of 60% overlap stereo pairs). In this case, we find bundle adjustment is most successful when the joint optimization of the cameras is performed initially for each flight line separately, then a subsequent bundle adjustment is invoked to jointly refine the cameras in all flight lines, improving the co-registration accuracy between the flight lines. We orthorectified the photographs using the optimized camera parameters and the pre-earthquake and post-earthquake DEMs produced using the photographs themselves. The final ground resolution of the orthophotos and DEMs is 1 m.

3.2. Extraction of Horizontal and Vertical Displacement Field Components

Once the pre-earthquake and post-earthquake orthomosaics are created using ASP, we measured the lateral coseismic displacements using COSI-Corr (Ajlou et al., 2021; Leprince et al., 2007; Milliner et al., 2015). We used a multiscale sliding correlation window of 256 by 256 pixels to 32 by 32 pixels for the correlation, with a step size of eight pixels, resulting in 8 m-resolution images that represent the eastward and northward components of displacement.

We measured the vertical coseismic displacement field using the pre-earthquake and post-earthquake DEMs created using ASP; however, simply differencing the DEMs does not isolate the vertical component of displacement when there is also a horizontal component (e.g., Barnhart et al., 2019; Delorme et al., 2020; Oskin et al., 2012). In this study, we measured the vertical component by (a) downsampling the pre-earthquake and post-earthquake DEMs to the same grid as the COSI-Corr displacement maps. Using a MATLAB code, we then

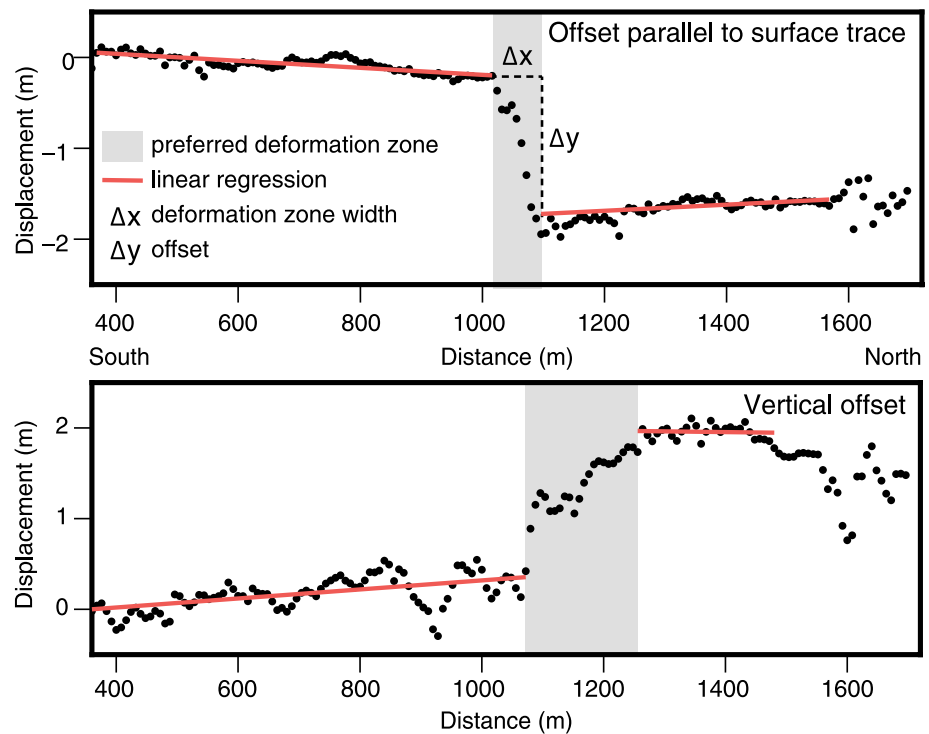


Figure 3. Example strike-perpendicular profile showing the fault trace-parallel and vertical components of the preferred deformation zone, linear regressions and offset (profile 16: see Figure S1 in Supporting Information S1).

calculated the vertical displacement for each pixel by (b) resampling and (c) warping the pre-earthquake DEM such that the pre-earthquake topography is shifted based on the amount of lateral coseismic displacement from our COSI-Corr displacement maps, then (d) subtracting this grid from the post-earthquake DEM.

We masked outliers and pixels where the optical image correlation signal-to-noise ratio is < 0.97 (Leprince et al., 2007). We used the detrending tool in COSI-Corr to remove a second-order polynomial trend which does not impact the near-field offset estimate, and corrected undulating artifacts by sampling the undulations away from the rupture and subtracting the average from the displacement field. We used the Non-Local Means tool in COSI-Corr to denoise the displacement field using a noise parameter of ~ 0.7 , a search area dimension of 21×21 pixels (168×168 m), and a patch size of 5×5 pixels (40×40 m). We estimate the precision of the resulting displacement field from the standard deviation in a stable area of the displacement maps as 0.16 m for the east-west component, 0.27 m for the north-south component, and 0.64 m for the vertical component.

3.3. Coseismic Offset and Distributed Deformation Measurements

To quantify offsets along the length of the main fault and secondary strands, we extract fault trace-parallel, -normal and vertical displacement profiles oriented perpendicular to the simplified fault traces at regular intervals along strike. For each profile, we first rotated the E-W and N-S displacements into components parallel and normal to the local fault strike. We consider secondary fault ruptures mapped in the field in the San Fernando area as separate, discrete fault strands rather than distributed deformation around the main fault strand (e.g., USGS Quaternary Fault and Fold Database, <https://doi.org/10.5066/F7S75FJM>; Barrows et al., 1975). The profiles are 2 km-long, are regularly-spaced 21 pixels (168 m) apart and are the average of 21 pixel-wide swaths such that each measurement is independent from its neighbors. We discarded the profiles for which the displacement trends are obscured by decorrelation or noise. In some areas that are decorrelated near the surface rupture, we use 25 pixel-wide swaths.

The offsets were measured by fitting linear regressions to the trends in displacement on either side of the fault (Figure 3 and Figure S2 in Supporting Information S1) and differencing the linear regression values at the near-fault extremities of the regression lines. Offset error was estimated by propagating the standard error of the

regression on either side of the fault. The regression line boundaries were picked manually, since displacement maps produced from historical optical imagery often have more noise than those produced with modern imaging systems including long wavelength trends and topographic artifacts, particularly for the vertical component in areas of variable topography (Ajlou et al., 2021). The displacement maps were also assessed for non-tectonic noise when choosing the trends used in the linear regressions. When it was unclear whether a signal is tectonic or noise, adjacent profiles were checked to confirm whether the feature is continuous. In some cases, the linear regressions end where the displacements start to deviate from their far-field trends. However, some profiles exhibit clear near-field inelastic deformation, and to better capture the full displacement in these cases, the linear regression sampled this trend only where continuous across at least five adjacent pixels. Secondary surface ruptures mapped in the field are considered to be discrete faults, and their offsets are measured separately, even where manifest on the same profile (the target fault is located approximately in the middle of each profile).

Preferred deformation zone widths were defined as the distance between the two regression line end-points on either side of the fault. Though we treat these measurements as rough approximations, they do show that some deformation zones are wider than others by an order of magnitude (Figure 3 and Figure S2 in Supporting Information S1). Preferred deformation zone widths were not determined in profiles with excessive decorrelation near the fault zone or where displacement trends on either side of the fault were too gradual to choose a preferred width.

We measured the magnitude of OFD at each profile by subtracting the maximum localized offsets measured in the field located within one profile swath from the total offset measured by profiling the displacement field either side of the fault zone. We normalized the OFD value to the total offset to obtain the percentage of off-fault deformation (%OFD). The OFD measurements presented in Figures 4b and 4c and Tables S2 and S3 in Supporting Information S1 include elastic and inelastic OFD (e.g., Milliner et al., 2015; Scott et al., 2018; Zinke et al., 2019). We did not attempt to isolate the inelastic component of deformation because the noise level and resolution of the data preclude us from reliably quantifying strain within the fault zone (e.g., Barnhart et al., 2019; Milliner et al., 2021; Scott et al., 2018). We used localized near-fault measurements taken from detailed field surveys conducted in the days following the earthquake that measured shortening, fault trace-parallel and vertical offsets (Baize et al., 2020; Barrows et al., 1973; Bonilla et al., 1971; Kamb et al., 1971; Sharp, 1975). In areas of highly distributed deformation, the field offset measurements reported are the cumulative displacement over a 50 m-wide (Kamb et al., 1971) or 200 m-wide zone (Bonilla et al., 1971), whereas elsewhere discrete offsets were measured on well-defined fault scarps. For the purpose of measuring %OFD, we chose field offset measurements within a 50 m-wide zone centered upon the primary fault break (e.g., Scott et al., 2018). The component of lateral offset perpendicular to the profile swath orientation is taken when calculating fault-trace parallel OFD. When only one or two of the three slip components were recorded in the field within a swath, we assumed that the remaining slip component(s) were imperceptible in the field within this swath and were given a value of 0.

4. Results

4.1. 3-D Coseismic Displacements

While seismic source models described shallow slip as pure reverse (Heaton, 1982; Heaton & Helmberger, 1979; Kim, 1989; Langston, 1978), the 3-D coseismic displacement results (Figure 2b) reveal a large component of left-lateral offset, consistent with previously published field and trilateration data (Bonilla et al., 1971; Kamb et al., 1971; Meade & Miller, 1973; Savage et al., 1975), but the higher spatial resolution obtained from image correlation and DEM differencing is indispensable for assessing the spatial distribution of near-field deformation and estimating the amount of OFD (Section 4.3). Precise measurements of postseismic deformation from repeat leveling and trilateration surveys indicate that afterslip was negligible compared to total slip, and below the detection threshold of the method used in this study (Savage & Church, 1975; Savage et al., 1975; Sylvester & Pollard, 1975). Some of the limitations of processing of historical aerial photographs are noticeable in Figure 2b; striping artifacts (north-south-oriented stripes in the east-west and vertical displacement components, east-west-oriented stripes in the north-south displacement component) were significantly, although not completely reduced. The north-south component of the tectonic signal is particularly affected by long-wavelength noise since the striping artifacts are roughly parallel to the fault rupture trace and difficult to reduce. This has a very limited impact on the vertical component of displacement since the topography in much of the study area is muted, and in the area of varied topography (in the San Gabriel Mountains), using the lateral displacements to extract the vertical component still reduces topographic noise. In all three dimensions, noise is much greater in

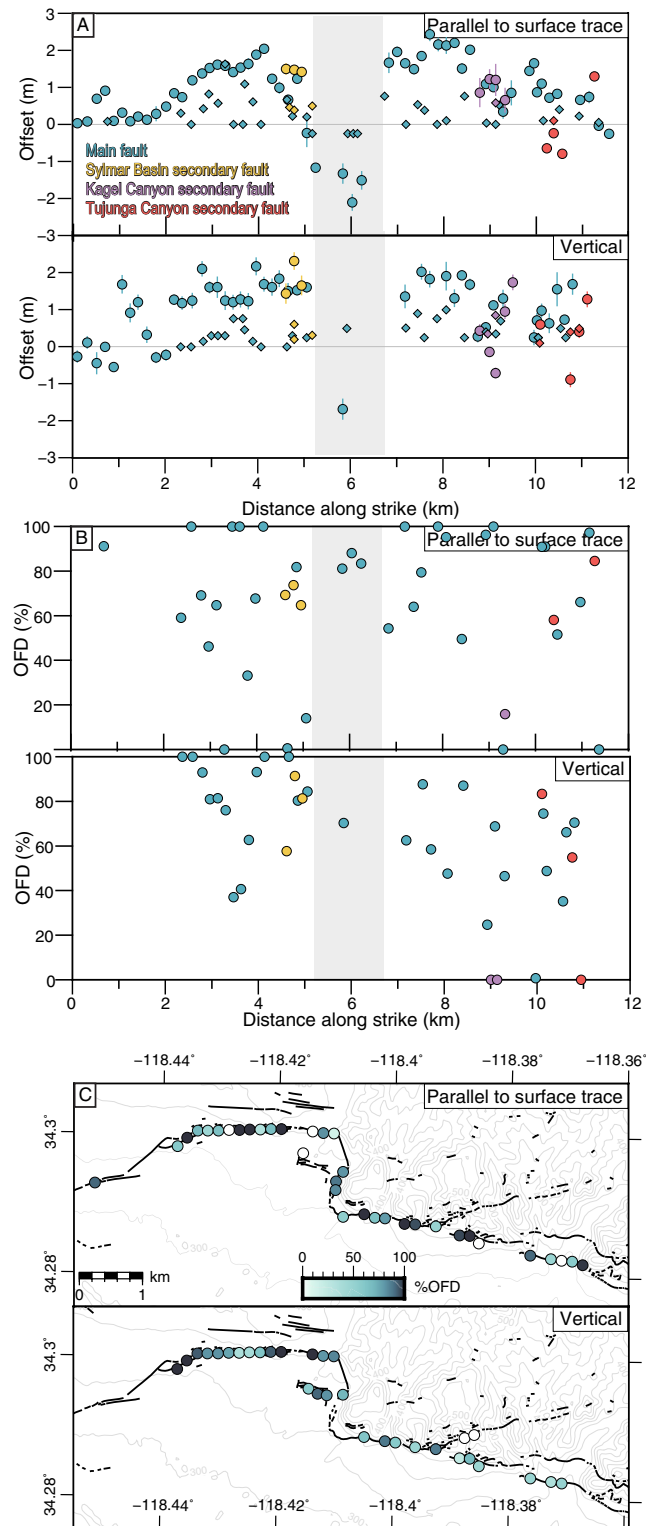


Figure 4. (a) Offset measurements plotted as a function of distance along the fault trace: left-lateral slip and hanging wall uplift are positive. Circles are offsets measured from displacement fields in Figure 2b and diamonds are field measurements (see Tables S2 and S3 in Supporting Information S1 for references). Shaded area represents the tear fault separating the Sylmar and Tujung sections of the main fault. (b) %OFD estimates as a function of distance along strike, where there are field offset measurements located within profile swaths of image correlation and DEM differencing displacement fields. (c) %OFD estimates plotted over fault trace.

the hanging wall of the Tujunga segment, likely introduced by the varied topography of the San Gabriel Mountains and anthropogenic changes that occurred between aerial photograph and reference DEM data acquisitions affecting the DEM generation and orthorectification steps. This heavily affected the region between longitudes -118.365 and -118.342 in the vertical component, and thus offsets were not measured in this area (Figure S3 in Supporting Information S1). The section of the San Fernando Fault shown in Figure 2b (the area used in this study) hosted the most slip and has a higher density of field measurements.

4.2. Near-Field Coseismic Offsets

All fault trace-perpendicular profiles with their deformation zone picks and linear regressions are included in Figure S2 in Supporting Information S1. While shortening is evident in the north-south displacement field, there are stripe artifacts near the fault (particularly in the footwall of the Tujunga segment). They introduce a gradual, long-wavelength signal to the fault-normal displacement profiles where long-wavelength OFD signals are expected and interferes with our ability to measure the total offset. Therefore, we focus on the fault-parallel and vertical components of displacement. Surface offsets on the Sylmar segment of the main fault rupture have roughly equal left-lateral and vertical components, reaching a maximum of 2.0 and 2.2 m, respectively, and 2.2 and 2.0 m in the Tujunga segment. The north-south tear fault connecting the two segments is dominated by right-lateral slip; however, a north-south zone of diffuse deformation ~ 800 m to the east is accommodating most of the vertical component of deformation at the bend connecting the Sylmar and Tujunga segments (Figure 2b). Barrows et al. (1975) mapped vertical deformation at this location but were unable to determine whether it occurred during the earthquake and most subsequent surface rupture maps do not include this detail (e.g., USGS Quaternary Fault and Fold Database, <https://doi.org/10.5066/F7S75FJM>). Determining that this deformation did occur during the 1971 earthquake demonstrates the effectiveness of historical image correlation in mapping complex coseismic surface deformation in greater detail. The largest left-lateral and vertical offsets in the Sylmar and Tujunga segments occur on the relatively straight parts of the fault where slip is not distributed onto secondary faults (Figures 2c and 4a). The Sylmar Basin secondary fault accommodates up to 1.5 and 2.3 m of left-lateral and vertical slip, respectively. The Kagel Canyon and Little Tujunga Canyon secondary fault offsets are irregular, with the former dominated by left-lateral slip while the latter is dominated by shortening.

The offsets increase gradually from the extremities of the study area toward the tear fault, plateauing for 1–2 km on either side of it, though in the Sylmar segment, the offset parallel to surface trace is distributed between the main fault and Sylmar Basin secondary fault (Figures 2c and 4a). The vertical offset at the Sylmar Basin secondary fault is a near-fault feature. The pattern of offsets along the fault trace is asymmetrical, with offsets tapering more gradually in the Tujunga segment, and according to field, leveling and trilateration surveys, continues to taper for ~ 6 km beyond the study area (Barrows et al., 1973; Bonilla et al., 1971; Meade & Miller, 1973; Savage et al., 1975).

4.3. Off-Fault Deformation

The average %OFD (\pm standard deviations) for the fault trace-parallel and vertical components are $69 \pm 33\%$, and $69 \pm 29\%$, respectively (Figure 4b). Since the Sylmar and Tujunga segments differ in terms of near-surface fault geometry, near-surface geological material, and surrounding topography, we assess the %OFD for the two segments separately. Fault trace-parallel %OFD is $65 \pm 34\%$ for the Sylmar segment and $70 \pm 34\%$ for the Tujunga segment. For the vertical component, average %OFD is larger for the Sylmar segment at $80 \pm 20\%$, with $53 \pm 29\%$ OFD for the Tujunga segment. The irregularity of %OFD measured in the fault trace-parallel orientation may reflect the challenges in measuring offsets in the field in an urban environment. On the geometrically simpler, straighter parts of the surface rupture where slip is not distributed onto secondary faults, %OFD in the fault trace-parallel orientation is still generally higher in the Tujunga segment than the Sylmar segment. Many of the offsets shown in the fault-perpendicular profiles are nonlinear, and have a different shape and width in the three dimensions at the same location, suggesting that different off-fault structures are accommodating different proportions of deformation in the dip slip and strike-slip orientations (Figure 3; Figure S2 in Supporting Information S1). In the fault-parallel component, there is little correlation between %OFD and total (profile-derived) offset; however, there is a weak positive correlation between %OFD and offset in the vertical component (Figure 5).

4.4. Width of Deformation Zone

In this section we present the average width of the zone of distributed deformation for the main rupture trace (using the “preferred” width measurement), then the averages and standard deviations of the Sylmar and Tujunga

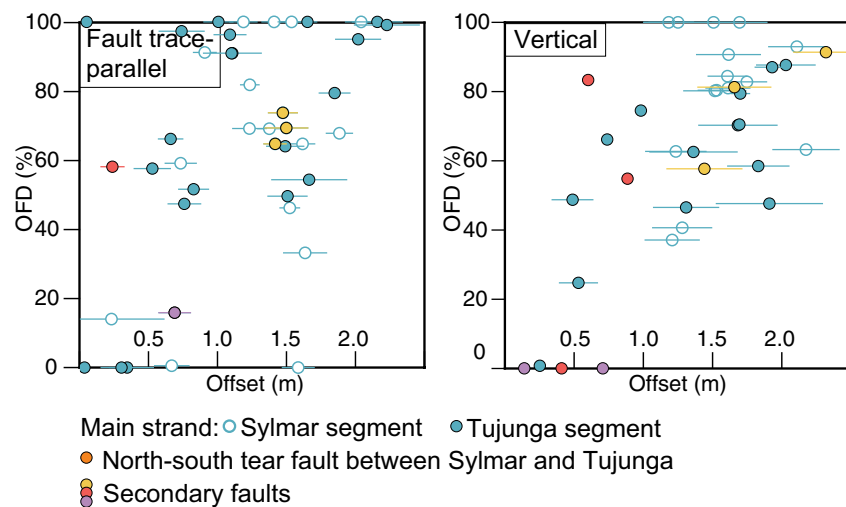


Figure 5. Comparison of %OFD and surface offset derived from fault-perpendicular profiles. Colors correspond to fault segments in Figure 2a.

segments of the main rupture trace separately. This additional step is taken because the width of diffuse deformation may be affected by attributes that differ between the two segments including near-surface fault geometry, near-surface geological material, surrounding topography. The average deformation zone width and standard deviations for the main rupture is 101 ± 70 m in the fault trace-parallel component, and 131 ± 79 m in the vertical component (Figure S4 in Supporting Information S1). Although there is a lot of scatter, the average width of the deformation zone of the fault trace-parallel component is narrower in the Sylmar segment than the Tujung segment (87 ± 54 m and 112 ± 82 m respectively). The Sylmar segment has a wider deformation zone on average in the vertical component (143 ± 76 m) compared to the Tujung segment (120 ± 84 m). While there is little correlation between %OFD and deformation width (Figure S5A in Supporting Information S1), there is a weak positive correlation between deformation width and offset (Figure S5B in Supporting Information S1).

The portion of offset accommodated by the hanging wall side of the field surface trace is generally distributed over a wider zone than the offset accommodated by the footwall side (Figure S2 in Supporting Information S1). However, there are a few areas where footwall deformation is more broadly distributed than hanging wall deformation over multiple consecutive profiles, in either parallel or vertical component, and these are located in areas of structural complexity. This occurs in main fault profiles 22 and 23 where the Sylmar segment deviates from its relatively straight trace over ~ 400 m, accommodated by multiple small structures at a high angle from the main fault (Figures S1 and S2 in Supporting Information S1; Barrows, 1975). The footwall deformation is wider in main fault profiles 46 and 47 where the Kagel secondary fault meets the main fault (Figures S1 and S2 in Supporting Information S1). The vertical displacements along nearby profile 44 also has a wider footwall deformation zone than most profiles, being approximately equal to the hanging wall deformation width. Profiles 57 to 61, located near a step-over, have approximately equal or wider hanging wall deformation widths (Figures S1 and S2 in Supporting Information S1; Barrows, 1975).

5. Discussion

We focus here on the vertical and fault trace-parallel components of deformation, since the striping artifacts in some areas obscure the horizontal shortening component, with particular attention given to the main fault strand.

5.1. Near-Surface Slip Distribution and Rotation of Rake Away From Pre-Stress Direction

Our results are consistent with previous studies in that offset measurements are generally highest and vary more smoothly on simpler, straighter segments of the main fault, and lower and more heterogeneous where there are small wavelength variations in fault trace orientation and where slip is partitioned onto secondary faults (Figures 2c and 4a; e.g., ; Ajourlou et al., 2021; Bruhat et al., 2020; Klinger et al., 2006; Manighetti et al., 2007; Milliner et al., 2015; Perrin et al., 2016). This suggests that structural complexity has a primary control on slip distribution.

Similar to field observations, fault trace-parallel and vertical surface offsets on the western half of the San Fernando rupture are roughly equal, however, those measured in this study are larger data (Barrows et al., 1973; Bonilla et al., 1971; Kamb et al., 1971; Sharp, 1975). Trilateration data indicated similarly large coseismic offsets, and the higher-resolution coseismic displacement fields presented in this paper confirm that much of this offset occurred on structures within hundreds of meters from the mapped surface rupture trace (Burford et al., 1971; Meade & Miller, 1973; Morrison, 1973; Savage et al., 1975). The left-lateral offset component contrasts with seismic source models that indicate that slip at depth was dominated by thrust faulting (e.g., Heaton, 1982; Langston, 1978). Furthermore, regional stress field estimations are inconsistent with the left-lateral surface slip, with the average compression axis oriented 16° from north, approximately perpendicular to the San Fernando fault strike (Stein et al., 1994, and references therein). Dynamic rupture modeling of pure thrust earthquakes reveals a small, temporary component of strike-slip motion induced near the edges of the rupture at shallow depths associated with the passage of the rupture front; however, the dip-slip component still dominates (Hempel et al., 2013; Kearsse & Kaneko, 2020). According to these models, the north-dipping San Fernando Fault would see a slight increase in left-lateral slip toward the western rupture termination and a slight increase in right-lateral slip toward the eastern rupture termination. The fault trace-parallel surface offset pattern of the San Fernando earthquake tells a different story, with left-lateral offset roughly equal to vertical offset in the western half, and on the eastern half, a left-lateral component that decreases toward the eastern termination (Figure S3 in Supporting Information S1; Barrows et al., 1973; Kahle, 1975).

This asymmetry may be partly due to the oblique (thrust/left-lateral) rake suggested by focal mechanisms determined by P-wave first motions (e.g., Whitcomb et al., 1973); however, the left-lateral component of slip is large enough at the eastern end that there may be an additional factor amplifying the left-lateral motion (Figure S3 in Supporting Information S1; Barrows et al., 1973). Additionally, Langston (1978); Heaton and Helmberger (1979); Heaton (1982); and Kim (1989) showed that the rupture evolving from oblique slip at depth to pure thrust in the shallower portion of the crust, aligning with the regional stress field (Stein et al., 1994), was more compatible with local and teleseismic data, suggesting that the left-lateral component of slip measured at the surface is too shallow to be resolved using seismic data (Figure 1). Guatteri and Spudich (1998) showed that the local slip direction can change when dynamic stresses radiated from elsewhere on the fault differ from the static prestress. This change is most likely when the prestress is heterogeneous, as expected for ruptures of geometrically-complex, immature faults like in the 1971 San Fernando earthquake (Bouchon, 1978). This can result in a temporal and spatial rotation in rake if the dynamic stresses are amplified enough near the free surface (Guatteri & Spudich, 1998; Oglesby, 2000).

In a surface-rupturing thrust earthquake such as this one, the dipping geometry of the fault amplifies the dynamic stresses in the hanging wall near the free surface and also enhances near-surface slip (Gabuchian et al., 2017; Oglesby, 2000). This amplification is consistent with the models proposed by Allen et al. (1998) and Brune (2001) for the San Fernando earthquake, which explain observations such as (a) the intense hanging wall ground shaking that launched a 50 m long piece of asphalt into the air during the earthquake (Boore, 1972; Maley & Cloud, 1971), (b) shattered earth on the hanging wall (Maley & Cloud, 1971; Nason, 1973), and 3) asymmetric static displacements measured by leveling surveys (Burford et al., 1971). The ground motion amplification in the hanging wall of a surface-rupturing thrust fault is due to geometric and dynamic effects, such as seismic waves propagating ahead of the rupture, reflecting off the free surface and back onto the fault (Oglesby, 2000; Oglesby & Day, 2001b). If the dynamic stresses near the surface did have a different direction than the static prestress, we would expect a temporal rotation in rake away from the static prestress direction due to the high ratio of dynamic to static stress magnitudes, until the dynamic stresses wane after the passage of the rupture front (Guatteri & Spudich, 1998; Kearsse & Kaneko, 2020; Oglesby & Day, 2001a). The temporal rotation in rake is consistent with reports of curved slickenlines found on some 1971 fault plane exposures, including ones near the eastern end of the surface rupture that recorded initial left-lateral slip then a rotation toward the prestress (thrust) slip direction (Kahle, 1975). Nevertheless, we cannot exactly account for the large-left-lateral component. Comparisons between static and dynamic rupture models may help determine whether increased slip on the western side of the study area occurred due to amplified dynamic stresses (e.g., Oglesby & Day, 2001b).

5.2. Factors Affecting % Off-Fault Deformation

Relatively immature faults are often associated with proportionally more distributed deformation (Dolan & Haravitch, 2014; Milliner et al., 2015; Perrin et al., 2016; Zinke et al., 2015), which is consistent with the generally high %OFD of the San Fernando Fault. However, the distribution of %OFD is different between the vertical

and fault trace-parallel components (Figures 3; 4B,C). The fault trace-parallel %OFD of the main fault is similar between the Sylmar and Tujunga segments while there is more of a difference in vertical %OFD between the two segments. Along the Sylmar segment, fault trace-parallel %OFD is 65%, compared to 80% for the vertical component, and along the Tujunga segment, the fault trace-parallel component's %OFD is 70%, compared to 53% for the vertical component. The increased scatter in %OFD measurements compared to the offsets measured from the optical image correlation and DEM differencing displacement fields is due to scatter in the field measurements, reflecting the increasing irregularity of offsets near the fault (e.g., Gold et al., 2019, 2021; Milliner et al., 2015; Scott et al., 2018) and uncertainties related to field data collection. For instance, greater fault trace-parallel offsets may be measured where there are features cross-cutting the fault such as roads, sidewalks and fences. The surface trace of the Sylmar segment is centered in the neighborhood of Sylmar, but the surface trace of the Tujunga segment is located at the edge of the urban area. Lateral offsets were likely less perceptible and more prone to underestimation in areas where the surface trace is located in the foothills of the San Gabriel Mountains. In the following paragraphs we discuss other possibilities that may have further impacted the fault trace-parallel and vertical components of %OFD.

Near-surface geology may have a primary control over the vertical component of %OFD, with greater average %OFD in the Sylmar segment of the main fault where it cuts through a thick package of sediments including partially indurated Pliocene-Pleistocene formations, based on studies integrating of geologic, geophysical, and oil well data (Langenheim et al., 2011). Vertical %OFD is lower in the Tujunga segment, which cuts through an older, stronger and thinner package of sedimentary rock than the Sylmar segment (Langenheim et al., 2011; Levi & Yeats, 1993). Structural complexity may also be a factor in the distribution of %OFD in the vertical component particularly along the Sylmar segment, with higher %OFD on the main fault near the segment boundaries and near macroscopic bends (Figures 4b and 4c). The difference in hanging wall topography between the Sylmar and Tujunga segment may imply a difference in slip rate, which is sometimes used as a metric for fault maturity which in turn may impact the %OFD as well (Dolan & Haravitch, 2014). Unlike for the vertical component of %OFD, near-surface geology and macroscopic fault corrugations do not appear to be primary controls in the fault trace-parallel component, with the Tujunga segment %OFD slightly higher than that of the Sylmar segment and no clear correlation with fault trace complexity (Figures 4b and 4c). Moreover, %OFD does not seem to scale with offset magnitude in the fault-parallel component, while there is a positive correlation in the vertical component (Figure 5).

A zone of broadly distributed deformation mapped in the hanging wall of the Sylmar segment possibly due to fold-related secondary faults may have affected the vertical component of %OFD (e.g., Allmendinger, 1998; Barrows, 1975; Gold et al., 2019). The strong dynamic stresses may have influenced the distribution of deformation as well, and may explain some of the differences between the vertical and fault trace-parallel components. The short-lived dynamic effects include damage due to seismic waves propagating ahead of the rupture front (Ma, 2008; Thomas & Bhat, 2018) and sudden and short-lived increases in normal stress, shear stress, strain rate, slip rate and rupture velocity around the rupture front (Andrews, 1976; Poliakov et al., 2002; Rice et al., 2005). After the passage of the rupture front, generation of OFD continues at generally lower stresses and strains (Thomas & Bhat, 2018) as slip progresses on the fault, since geometric complexities will locally increase the stress field enough to initiate cracking in the damage zone (Chester & Chester, 2000; Dieterich & Smith, 2009). The previously mentioned temporal rake rotation may explain the different OFD behaviors in the fault trace-parallel and vertical components. If most of the left-lateral near-surface offset resulted from transient dynamic effects, most of the fault trace-parallel OFD would have been generated as a result of the high stress and strain rates associated with the passage of the rupture front. Compared to the Sylmar segment, the left-lateral %OFD in the Tujunga segment may have been enhanced by greater ground motion amplification due its much shallower dip and greater hanging wall topography (Boore, 1973; Oglesby, 2000). While some of the vertical component of OFD would have likely been generated during the very short dynamic stress stage, some of the OFD will have accumulated as the slip vector rotated toward the prestress (thrust) direction and continued slipping. These very different conditions under which %OFD develops result in different micro- and macro-rack orientations, spatial patterns and magnitudes of %OFD. As a result, much of the left-lateral and vertical components of OFD may have been accommodated on separate structures, as suggested by differing shapes and gradients of the fault trace-parallel and vertical displacement profiles (e.g., Figure 3; Figure S2 in Supporting Information S1; Aben et al., 2020; Chester & Chester, 2000; Griffith et al., 2010; Templeton & Rice, 2008; Yamashita, 2000). Dynamic rupture models suggest that OFD generated by dynamic stresses is influenced by

fault roughness (and by extension fault maturity) and by the strength of near-surface materials (Roten et al., 2017; Wollherr et al., 2019). However, comparison between the different components of slip is limited by the unreliable fault trace-perpendicular offsets in the optical image correlation displacement field.

The poor correlation between %OFD and deformation zone width suggests that these measures have different controls resulting in OFD that can be distributed over different deformation zone widths (Figure S5A in Supporting Information S1). For example, the density of off-fault microfractures near the fault core may influence the deformation zone width for a given %OFD. Localized, near-fault offsets are also more irregular than farther-field offsets, affecting the %OFD estimation and introducing some of the scatter into Figure S5A in Supporting Information S1 (e.g., Gold et al., 2019, 2021; Milliner et al., 2015; Scott et al., 2018). This scatter may reflect the increase in complexity near the fault core and the challenges in measuring offsets in the field. The Sylmar segment deformation zone measured from the fault trace-parallel displacement field is generally wider than that of the Tujunga segment, suggesting that near-surface materials may have a primary control on deformation zone width in the fault trace-parallel orientation, while this does not seem to be the case for %OFD. The wider deformation zone in the vertical orientation may be due to greater noise level of the DEMs than the optical image correlations, wider deformation caused by progressive slip on a rough surface, more cumulative slip in the thrust than fault trace-parallel direction (Faulkner et al., 2011; Mitchell & Faulkner, 2009), or perhaps a reduction in the thrust component of slip near the surface (Gold et al., 2019).

6. Conclusions

While most studies on slip localization focus on strike-slip earthquakes, stereo photographs and advances in image processing enabled the production of displacement maps capturing the fault-trace parallel and vertical components of coseismic deformation from the 1971 San Fernando oblique thrust earthquake. The results have important implications for the characterization of the fault for seismic hazard assessments, with some offsets distributed over a wide zone (>200 m) and a greater component of left-lateral surface offset than expected from moment tensor inversions and finite fault modeling (e.g., Heaton, 1982; Kim, 1989; Langston, 1978). The rotation of the slip vector near the surface may have occurred as a transient dynamic effect based on the amplification of dynamic stresses associated with surface-rupturing thrust faults (Gautteri & Spudich, 1998; Oglesby, 2000), consistent both with the presence of curved slickenlines (Kahle, 1975; Kearsse & Kaneko, 2020) and with previous models that attempted to explain the intense ground motions of the San Fernando earthquake (Allen et al., 1998; Boore, 1973). Furthermore, the displacement maps show that dip slip and strike slip were partitioned on different secondary structures, some of which are not present in most rupture maps of this area. This study suggests that in oblique thrust/reverse faults, the fault-trace parallel and vertical components of OFD can be partitioned. For surface-rupturing dip-slip faults, it is worth considering near-surface dip and topography as factors that can amplify hanging wall ground motions and OFD. However, further work is needed to investigate the OFD patterns caused by processes such as the amplification of dynamic stresses and slip on a rough surface and whether they are more strongly influenced by different factors.

Data Availability Statements

Scanned aerial photographs were obtained from the United States Geological Survey's Center for Earth Resources Observation and Science (EROS; <http://earthexplorer.usgs.gov>). Ames Stereo Pipeline (Beyer et al., 2018) and COSI-Corr (Leprince et al., 2007) were used for data processing. The digital elevation models and displacement maps produced are available at <https://doi.org/10.5281/zenodo.7327824>. The figures in this paper were generated using Generic Mapping Tools (Wessell et al., 2013). Offsets measured in the field used to calculate off-fault deformation are from Bonilla et al. (1971); Kamb et al. (1971); Barrows et al. (1973); Baize et al. (2020).

References

- Aben, F. M., Brantut, N., & Mitchell, T. M. (2020). Off-fault damage characterization during and after experimental quasi-static and dynamic rupture in crustal rock from laboratory P wave tomography and microstructures. *Journal of Geophysical Research: Solid Earth*, 125(8), e2020JB019860. <https://doi.org/10.1029/2020jb019860>
- Ajorlou, N., Hollingsworth, J., Mousavi, Z., Ghods, A., & Masoumi, Z. (2021). Characterizing near-field surface deformation in the 1990 Rudbar Earthquake (Iran) using optical image correlation. *Geochemistry, Geophysics, Geosystems*, 22(6), e2021GC009704. <https://doi.org/10.1029/2021gc009704>

Acknowledgments

E. G. was funded through an Alexander Graham Bell Canada Graduate Scholarship and Michael Smith Foreign Study Supplement from the Natural Sciences and Engineering Research Council of Canada, and a Montalbano Scholars Fellowship and President's Research Scholarship, both from University of Victoria. E. N. was supported by a Canada Research Chair and grants from the Natural Sciences and Engineering Research Council of Canada (NSERC Discovery Grant 2017-04029), the Canada Foundation for Innovation, and the BC Knowledge Development Fund. J.H. was supported by grants from CNES and BQR. G.F. was supported by SCEC Award 21128. We are grateful for thorough reviews from Katherine Scharer and an anonymous reviewer, which greatly improved the manuscript. We also thank Editor in Chief Isabelle Manighetti and an associate editor for their valuable and constructive comments.

- Allen, C. R., Brune, J. N., Cluff, L. S., & Barrows, A. G., Jr. (1998). Evidence for unusually strong near-field ground motion on the hanging wall of the San Fernando fault during the 1971 earthquake. *Seismological Research Letters*, 69(6), 524–531. <https://doi.org/10.1785/gssrl.69.6.524>
- Allmendinger, R. W. (1998). Inverse and forward numerical modeling of trishear fault-propagation folds. *Tectonics*, 17(4), 640–656. <https://doi.org/10.1029/98tc01907>
- Andrews, D. (1976). Rupture velocity of plane strain shear cracks. *Journal of Geophysical Research*, 81(32), 5679–5687. <https://doi.org/10.1029/jb081i032p05679>
- Antoine, S. L., Klinger, Y., Delorme, A., Wang, K., Bürgmann, R., & Gold, R. D. (2021). Diffuse deformation and surface faulting distribution from submetric image correlation along the 2019 Ridgecrest, California, ruptures. *Bulletin of the Seismological Society of America*, 111(5), 2275–2302. <https://doi.org/10.1785/0120210036>
- Baize, S., Nurminen, F., Sarmiento, A., Dawson, T., Takao, M., Scotti, O., et al. (2020). A worldwide and unified database of surface ruptures (SURE) for fault displacement hazard analyses. *Seismological Research Letters*, 91(1), 499–520. <https://doi.org/10.1785/0220190144>
- Barker, J. S., & Langston, C. A. (1982). Moment tensor inversion of complex earthquakes. *Geophysical Journal International*, 68(3), 777–803. <https://doi.org/10.1111/j.1365-246x.1982.tb04928.x>
- Barnhart, W. D., Gold, R. D., Shea, H. N., Peterson, K. E., Briggs, R. W., & Harbor, D. J. (2019). Vertical coseismic offsets derived from high-resolution stereogrammetric DSM differencing: The 2013 Baluchistan, Pakistan earthquake. *Journal of Geophysical Research*, 124(6), 6039–6055. <https://doi.org/10.1029/2018JB017107>
- Barrows, A. G. (1975). Surface effects and related geology of the San Fernando earthquake in the foothill region between Little Tujunga and Wilson Canyons. In G. Oakeshott (Ed.), *San Fernando earthquake of 9 February 1971* (Vol. 196, pp. 97–117). California Division of Mines and Geology.
- Barrows, A. G., Kahle, J. E., Weber, F. H., & Saul, R. (1973). Map of surface breaks resulting from the San Fernando, California, earthquake. In L. Murphy (Ed.), *San Fernando, California, earthquake of February 9* (Vol. 3, pp. 127–134). U.S. Department of Commerce, National Oceanic and Atmospheric Administration 1971.
- Barrows, A. G., Kahle, J. E., Weber, F. H., Saul, R., & Morton, D. (1975). Surface effects map of the San Fernando Earthquake area (scale 1:24,000). In G. Oakeshott (Ed.), *San Fernando earthquake of 9 February 1971, Plate 3* (Vol. 196). California Division of Mines and Geology.
- Ben-Zion, Y., & Sammis, C. G. (2003). Characterization of fault zones. *Pure and Applied Geophysics*, 160(3–4), 677–715. <https://doi.org/10.1007/PL00012554>
- Berryman, K. R., Cochran, U. A., Clark, K. J., Biasi, G. P., Langridge, R. M., & Villamor, P. (2012). Major earthquakes occur regularly on an isolated plate boundary fault. *Science*, 336(6089), 1690–1693. <https://doi.org/10.1126/science.1218959>
- Beyer, R. A., Alexandrov, O., & McMichael, S. (2018). The Ames Stereo Pipeline: NASA's open source software for deriving and processing terrain data. *Earth and Space Science*, 5(9), 537–548. <https://doi.org/10.1029/2018ea000409>
- Bonilla, M. (1973). Trench exposures across surface fault ruptures associated with San Fernando Earthquake. In L. Murphy (Ed.), *San Fernando, California, earthquake of February 9* (Vol. 3, pp. 173–182). U.S. Department of Commerce, National Oceanic and Atmospheric Administration 1971.
- Bonilla, M. G., Buchanan, J. M., Castle, R., Clark, M. M., Frizzell, V. A., Gulliver, R. M., et al. (1971). Surface faulting. In *The San Fernando, California earthquake of February 9th* (pp. 56–76). U.S. Geological Survey Professional Paper 733.
- Boore, D. M. (1972). A note on the effect of simple topography on seismic SH waves. *Bulletin of the Seismological Society of America*, 62(1), 275–284. <https://doi.org/10.1785/bssa0620010275>
- Boore, D. M. (1973). The effect of simple topography on seismic waves: Implications for the accelerations recorded at Pacoima Dam, San Fernando Valley, California. *Bulletin of the Seismological Society of America*, 63(5), 1603–1609. <https://doi.org/10.1785/bssa0630051603>
- Bouchon, M. (1978). A dynamic source model for the San Fernando earthquake. *Bulletin of the Seismological Society of America*, 68(6), 1555–1576. <https://doi.org/10.1785/bssa0680061555>
- Bruhat, L., Fang, Z., & Dunham, E. M. (2016). Rupture complexity and the supershear transition on rough faults. *Journal of Geophysical Research: Solid Earth*, 121(1), 210–224. <https://doi.org/10.1002/2015jb012512>
- Bruhat, L., Klinger, Y., Vallage, A., & Dunham, E. M. (2020). Influence of fault roughness on surface displacement: From numerical simulations to coseismic slip distributions. *Geophysical Journal International*, 220(3), 1857–1877. <https://doi.org/10.1093/gji/ggz545>
- Brune, J. N. (2001). Shattered rock and precarious rock evidence for strong asymmetry in ground motions during thrust faulting. *Bulletin of the Seismological Society of America*, 91(3), 441–447. <https://doi.org/10.1785/0120000118>
- Burford, R., Castle, R., Church, J., Kinoshita, S., Kirby, S., Ruthven, R., & Savage, J. (1971). Preliminary measurements of tectonic movement. In *The San Fernando, California earthquake of February 9th* (pp. 80–85). U.S. Geological Survey Professional Paper 733.
- Burgette, R. J., Hanson, A. M., Scharer, K. M., Rittenour, T. M., & McPhillips, D. (2020). Late Quaternary slip rate of the Central Sierra Madre fault, southern California: Implications for slip partitioning and earthquake hazard. *Earth and Planetary Science Letters*, 530, 115907. <https://doi.org/10.1016/j.epsl.2019.115907>
- Bürgmann, R., Pollard, D. D., & Martel, S. J. (1994). Slip distributions on faults: Effects of stress gradients, inelastic deformation, heterogeneous host-rock stiffness, and fault interaction. *Journal of Structural Geology*, 16(12), 1675–1690. [https://doi.org/10.1016/0191-8141\(94\)90134-1](https://doi.org/10.1016/0191-8141(94)90134-1)
- Carena, S., & Suppe, J. (2002). Three-dimensional imaging of active structures using earthquake aftershocks: The Northridge thrust, California. *Journal of Structural Geology*, 24(4), 887–904. [https://doi.org/10.1016/S0191-8141\(01\)00110-9](https://doi.org/10.1016/S0191-8141(01)00110-9)
- Cheng, G., & Barnhart, W. D. (2021). Permanent co-seismic deformation of the 2013 Mw7.7 Baluchistan, Pakistan earthquake from high-resolution surface strain analysis. *Journal of Geophysical Research: Solid Earth*, 126(3), e2020JB020622. <https://doi.org/10.1029/2020jb020622>
- Chester, F. M., & Chester, J. S. (2000). Stress and deformation along wavy frictional faults. *Journal of Geophysical Research*, 105(B10), 23421–23430. <https://doi.org/10.1029/2000jb900241>
- Cochran, E. S., Li, Y. G., Shearer, P. M., Barbot, S., Fialko, Y., & Vidale, J. E. (2009). Seismic and geodetic evidence for extensive, long-lived fault damage zones. *Geology*, 37(4), 315–318. <https://doi.org/10.1130/G25306A.1>
- Delorme, A., Grandin, R., Klinger, Y., Pierrot-Deseilligny, M., Feuillet, N., Jacques, E., et al. (2020). Complex deformation at shallow depth during the 30 October 2016 Mw6.5 Norcia earthquake: Interference between tectonic and gravity processes? *Tectonics*, 39(2), e2019TC005596. <https://doi.org/10.1029/2019tc005596>
- Dieterich, J. H., & Smith, D. E. (2009). Nonplanar faults: Mechanics of slip and off-fault damage. In *Mechanics, structure and evolution of fault zones* (pp. 1799–1815). Springer. https://doi.org/10.1007/978-3-0346-0138-2_12
- Dolan, J. F., & Haravitch, B. D. (2014). How well do surface slip measurements track slip at depth in large strike-slip earthquakes? The importance of fault structural maturity in controlling on-fault slip versus off-fault surface deformation. *Earth and Planetary Science Letters*, 388, 38–47. <https://doi.org/10.1016/j.epsl.2013.11.043>
- Faulkner, D., Mitchell, T., Jensen, E., & Cembrano, J. (2011). Scaling of fault damage zones with displacement and the implications for fault growth processes. *Journal of Geophysical Research*, 116(B5), B05403. <https://doi.org/10.1029/2010jb007788>

- Fialko, Y., Sandwell, D., Agnew, D., Simons, M., Shearer, P., & Minster, B. (2002). Deformation on nearby faults induced by the 1999 Hector Mine earthquake. *Science*, 297(5588), 1858–1862. <https://doi.org/10.1126/science.1074671>
- Fialko, Y., Sandwell, D., Simons, M., & Rosen, P. (2005). Three-dimensional deformation caused by the Bam, Iran, earthquake and the origin of shallow slip deficit. *Nature*, 435(7040), 295–299. <https://doi.org/10.1038/nature03425>
- Fuis, G. S., Clayton, R. W., Davis, P. M., Ryberg, T., Lutter, W. J., Okaya, D. A., et al. (2003). Fault systems of the 1971 San Fernando and 1994 Northridge earthquakes, southern California: Relocated aftershocks and seismic images from LARSE II. *Geology*, 31(2), 171. [https://doi.org/10.1130/0091-7613\(2003\)031<0171:fsotsf>2.0.co;2](https://doi.org/10.1130/0091-7613(2003)031<0171:fsotsf>2.0.co;2)
- Gabuchian, V., Rosakis, A. J., Bhat, H. S., Madariaga, R., & Kanamori, H. (2017). Experimental evidence that thrust earthquake ruptures might open faults. *Nature*, 545(7654), 336–339. <https://doi.org/10.1038/nature22045>
- Gaudreau, É., Nissen, E. K., Bergman, E. A., Benz, H. M., Tan, F., & Karasözen, E. (2019). The August 2018 Kaktovik earthquakes: Active tectonics in Northeastern Alaska revealed with InSAR and Seismology. *Geophysical Research Letters*, 46(24), 14412–14420. <https://doi.org/10.1029/2019GL085651>
- Gold, R. D., Clark, D., Barnhart, W. D., King, T., Quigley, M., & Briggs, R. W. (2019). Surface rupture and distributed deformation revealed by optical satellite imagery: The intraplate 2016 M_w 6.0 Petermann Ranges earthquake, Australia. *Geophysical Research Letters*, 46, 10394–10403. <https://doi.org/10.1029/2019GL084926>
- Gold, R. D., DuRoss, C. B., & Barnhart, W. D. (2021). Coseismic surface displacement in the 2019 Ridgecrest earthquakes: Comparison of field measurements and optical image correlation results. *Geochemistry, Geophysics, Geosystems*, 22(3), e09326. <https://doi.org/10.1029/2020GC009326>
- Griffith, W. A., Nielsen, S., Di Toro, G., & Smith, S. A. (2010). Rough faults, distributed weakening, and off-fault deformation. *Journal of Geophysical Research*, 115(B8), B08409. <https://doi.org/10.1029/2009jb006925>
- Guatterri, M., & Spudich, P. (1998). Coseismic temporal changes of slip direction: The effect of absolute stress on dynamic rupture. *Bulletin of the Seismological Society of America*, 88(3), 777–789. <https://doi.org/10.1785/bssa0880030777>
- Hampel, A., Li, T., & Maniatis, G. (2013). Contrasting strike-slip motions on thrust and normal faults: Implications for space-geodetic monitoring of surface deformation. *Geology*, 41(3), 299–302. <https://doi.org/10.1130/G33927.1>
- Harrington, R. M., & Brodsky, E. E. (2009). Source duration scales with magnitude differently for earthquakes on the San Andreas Fault and on secondary faults in Parkfield, California. *Bulletin of the Seismological Society of America*, 99(4), 2323–2334. <https://doi.org/10.1785/0120080216>
- Heath, E. G., & Leighton, F. B. (1973). Subsurface investigation of ground rupturing during San Fernando earthquake. In L. Murphy (Ed.), *San Fernando, California, earthquake of February 9* (Vol. 3, pp. 165–172). U.S. Department of Commerce, National Oceanic and Atmospheric Administration 1971.
- Heaton, T. H. (1982). The 1971 San Fernando earthquake: A double event? *Bulletin of the Seismological Society of America*, 72(6A), 2037–2062. <https://doi.org/10.1785/bssa07206a2037>
- Heaton, T. H., & Helmlinger, D. V. (1979). Generalized ray models of the San Fernando earthquake. *Bulletin of the Seismological Society of America*, 69(5), 1311–1341.
- Huang, Y. (2018). Earthquake rupture in fault zones with along-strike material heterogeneity. *Journal of Geophysical Research: Solid Earth*, 123(11), 9884–9898. <https://doi.org/10.1029/2018jb016354>
- Jackson, J., Bouchon, M., Fielding, E., Funning, G., Ghorashi, M., Hatzfeld, D., et al. (2006). Seismotectonic, rupture process, and earthquake-hazard aspects of the 2003 December 26 Bam, Iran, earthquake. *Geophysical Journal International*, 166(3), 1270–1292. <https://doi.org/10.1111/j.1365-246x.2006.03056.x>
- Jara, J., Bruhat, L., Thomas, M. Y., Antoine, S. L., Okubo, K., Rougier, E., et al. (2021). Signature of transition to supershear rupture speed in the coseismic off-fault damage zone. *Proceedings of the Royal Society A*, 477(2255), 20210364. <https://doi.org/10.1098/rspa.2021.0364>
- Kahle, J. E. (1975). Surface effects and related geology of the Lakeview fault segment of the San Fernando fault zone. In G. Oakeshott (Ed.), *San Fernando earthquake of 9 February 1971* (Vol. 196, pp. 119–135). California Division of Mines and Geology.
- Kamb, B., Silver, L., Abrams, L., Carter, B., Jordan, T., & Minster, J. (1971). Pattern of faulting and nature of fault movement in the San Fernando earthquake. In *The San Fernando* (pp. 41–55). California Earthquake of February 9th. U.S. Geological Survey Professional Paper 733.
- Kaneko, Y., & Fialko, Y. (2011). Shallow slip deficit due to large strike-slip earthquakes in dynamic rupture simulations with elasto-plastic off-fault response. *Geophysical Journal International*, 186(3), 1389–1403. <https://doi.org/10.1111/j.1365-246x.2011.05117.x>
- Kearse, J., & Kaneko, Y. (2020). On-fault geological fingerprint of earthquake rupture direction. *Journal of Geophysical Research*, 125(9), e19863. <https://doi.org/10.1029/2020JB019863>
- Kim, J. (1989). *Complex seismic sources and time-dependent moment tensor inversion (Unpublished doctoral dissertation)*. University of Arizona.
- Klinger, Y., Michel, R., & King, G. (2006). Evidence for an earthquake barrier model from Mw 7.8 Kokoxili (Tibet) earthquake slip-distribution. *Earth and Planetary Science Letters*, 242(3–4), 354–364. <https://doi.org/10.1016/j.epsl.2005.12.003>
- Langenheim, V. E., Wright, T. L., Okaya, D. A., Yeats, R. S., Fuis, G. S., Thygesen, K., & Thybo, H. (2011). Structure of the San Fernando Valley region, California: Implications for seismic hazard and tectonic history. *Geosphere*, 7(2), 528–572. <https://doi.org/10.1130/GES00597.1>
- Langston, C. A. (1978). The February 9, 1971 San Fernando earthquake: A study of source finiteness in teleseismic body waves. *Bulletin of the Seismological Society of America*, 68(1), 1–29. <https://doi.org/10.1785/bssa0680010001>
- Leprince, S., Barbot, S., Ayoub, F., & Avouac, J.-P. (2007). Automatic and precise orthorectification, coregistration, and subpixel correlation of satellite images, application to ground deformation measurements. *IEEE Transactions on Geoscience and Remote Sensing*, 45(6), 1529–1558. <https://doi.org/10.1109/TGRS.2006.888937>
- Levi, S., & Yeats, R. S. (1993). Paleomagnetic constraints on the initiation of uplift on the Santa Susana Fault, Western Transverse Ranges, California. *Tectonics*, 12(3), 688–702. <https://doi.org/10.1029/93TC00133>
- Lindvall, S. C., & Rubin, C. M. (2008). *Slip rate studies along the Sierra Madre-Cucamonga fault system using geomorphic and cosmogenic surface exposure age constraints: Collaborative research with Central Washington University and William Lettis & Associates, Inc. Final Technical Report* (p. 13). NEHRP External Grant Award Number 03HQGR0084.
- Lockner, D., Byerlee, J., Kuksenko, V., Ponomarev, A., & Sidorin, A. (1991). Quasi-static fault growth and shear fracture energy in granite. *Nature*, 350(6313), 39–42. <https://doi.org/10.1038/350039a0>
- Lyakhovskiy, V., Ben-Zion, Y., & Agnon, A. (1997). Distributed damage, faulting, and friction. *Journal of Geophysical Research*, 102(B12), 27635–27649. <https://doi.org/10.1029/97jb01896>
- Ma, S. (2008). A physical model for widespread near-surface and fault zone damage induced by earthquakes. *Geochemistry, Geophysics, Geosystems*, 9(11), Q11009. <https://doi.org/10.1029/2008GC002231>
- Maley, R., & Cloud, W. (1971). Preliminary strong-motion results from the San Fernando earthquake of February 9, 1971. In *The San Fernando, California earthquake of February 9th* (pp. 163–176). U.S. Geological Survey Professional Paper 733.

- Manighetti, I., Campillo, M., Bouley, S., & Cotton, F. (2007). Earthquake scaling, fault segmentation, and structural maturity. *Earth and Planetary Science Letters*, 253(3–4), 429–438. <https://doi.org/10.1016/j.epsl.2006.11.004>
- Manighetti, I., Mercier, A., & De Barros, L. (2021). Fault trace corrugation and segmentation as a measure of fault structural maturity. *Geophysical Research Letters*, 48(20), e2021GL095372. <https://doi.org/10.1029/2021gl095372>
- Martel, S. J., Pollard, D. D., & Segall, P. (1988). Development of simple strike-slip fault zones, Mount Abbot quadrangle, Sierra Nevada, California. *The Geological Society of America Bulletin*, 100(9), 1451–1465. [https://doi.org/10.1130/0016-7606\(1988\)100<1451:dossf>2.3.co;2](https://doi.org/10.1130/0016-7606(1988)100<1451:dossf>2.3.co;2)
- Meade, B. K., & Miller, R. W. (1973). Horizontal crustal movements determined from surveys after San Fernando Earthquake. In L. Murphy (Ed.), *San Fernando, California, earthquake of February 9* (Vol. 3, pp. 243–293). U.S. Department of Commerce, National Oceanic and Atmospheric Administration 1971.
- Milliner, C., Donnellan, A., Aati, S., Avouac, J.-P., Zinke, R., Dolan, J. F., et al. (2021). Bookshelf kinematics and the effect of dilatation on fault zone inelastic deformation: Examples from optical image correlation measurements of the 2019 Ridgecrest Earthquake sequence. *Journal of Geophysical Research: Solid Earth*, 126(3), e2020JB020551. <https://doi.org/10.1029/2020jb020551>
- Milliner, C. W. D., Dolan, J. F., Hollingsworth, J., Leprince, S., Ayoub, F., & Sammis, C. G. (2015). Quantifying near-field and off-fault deformation patterns of the 1992 M_w 7.3 Landers earthquake. *Geochemistry, Geophysics, Geosystems*, 16(5), 1577–1598. <https://doi.org/10.1002/2014GC005693>
- Mitchell, T., & Faulkner, D. (2009). The nature and origin of off-fault damage surrounding strike-slip fault zones with a wide range of displacements: A field study from the Atacama fault system, northern Chile. *Journal of Structural Geology*, 31(8), 802–816. <https://doi.org/10.1016/j.jsg.2009.05.002>
- Mori, J., Wald, D. J., & Wesson, R. L. (1995). Overlapping fault planes of the 1971 San Fernando and 1994 Northridge, California earthquakes. *Geophysical Research Letters*, 22(9), 1033–1036. <https://doi.org/10.1029/95GL00712>
- Morrison, N. L. (1973). Vertical crustal movements determined from surveys before and after San Fernando Earthquake. In L. Murphy (Ed.), *San Fernando, California, earthquake of February 9* (Vol. 3, pp. 295–324). U.S. Department of Commerce, National Oceanic and Atmospheric Administration 1971.
- Nason, R. D. (1973). Increased seismic shaking above a thrust fault. In G. Oakeshott, N. A. Benfer, J. L. Coffman, J. R. Bernick, & L. T. Dees (Eds.), *San Fernando, California, earthquake of 9, February 1971* (Vol. 3, pp. 123–126). U.S. Department of Commerce.
- Oglesby, D. D. (2000). The three-dimensional dynamics of dipping faults. *Bulletin of the Seismological Society of America*, 90(3), 616–628. <https://doi.org/10.1785/0119990113>
- Oglesby, D. D., & Day, S. M. (2001a). The effect of fault geometry on the 1999 Chi-Chi (Taiwan) earthquake. *Geophysical Research Letters*, 28(9), 1831–1834. <https://doi.org/10.1029/2000gl012043>
- Oglesby, D. D., & Day, S. M. (2001b). Fault geometry and the dynamics of the 1999 Chi-Chi (Taiwan) earthquake. *Bulletin of the Seismological Society of America*, 91(5), 1099–1111. <https://doi.org/10.1785/0120000714>
- Oskin, M. E., Arrowsmith, J. R., Corona, A. H., Elliott, A. J., Fletcher, J. M., Fielding, E. J., et al. (2012). Near-field deformation from the El Mayor–Cucapah earthquake revealed by differential LIDAR. *Science*, 335(6069), 702–705. <https://doi.org/10.1126/science.1213778>
- Perrin, C., Manighetti, I., Ampuero, J.-P., Cappa, F., & Gaudemer, Y. (2016). Location of largest earthquake slip and fast rupture controlled by along-strike change in fault structural maturity due to fault growth. *Journal of Geophysical Research: Solid Earth*, 121(5), 3666–3685. <https://doi.org/10.1002/2015jb012671>
- Poliakov, A. N., Dmowska, R., & Rice, J. R. (2002). Dynamic shear rupture interactions with fault bends and off-axis secondary faulting. *Journal of Geophysical Research*, 107(B11), ESE6-1–ESE6-18. <https://doi.org/10.1029/2001jb000572>
- Pousse-Beltran, L., Nissen, E., Bergman, E. A., Cambaz, M. D., Gaudreau, É., Karasözen, E., & Tan, F. (2020). The 2020 M_w 6.8 Elazığ (Turkey) earthquake reveals rupture behavior of the East Anatolian Fault. *Geophysical Research Letters*, 47(13), e2020GL088136. <https://doi.org/10.1029/2020GL088136>
- Proctor, R., Crook, J. R., McKeown, M., & Moresco, R. (1972). Relation of known faults to surface ruptures, 1971 San Fernando earthquake, southern California. *The Geological Society of America Bulletin*, 83(6), 1601–1618. [https://doi.org/10.1130/0016-7606\(1972\)83:1601:rokfts\]2.0.co;2](https://doi.org/10.1130/0016-7606(1972)83:1601:rokfts]2.0.co;2)
- Quigley, M., Van Dissen, R., Litchfield, N., Villamor, P., Duffy, B., Barrell, D., et al. (2012). Surface rupture during the 2010 M_w 7.1 Darfield (Canterbury) earthquake: Implications for fault rupture dynamics and seismic-hazard analysis. *Geology*, 40(1), 55–58. <https://doi.org/10.1130/g32528.1>
- Radiguet, M., Cotton, F., Manighetti, I., Campillo, M., & Douglas, J. (2009). Dependency of near-field ground motions on the structural maturity of the ruptured faults. *Bulletin of the Seismological Society of America*, 99(4), 2572–2581. <https://doi.org/10.1785/0120080340>
- Rice, J. R., Sammis, C. G., & Parsons, R. (2005). Off-fault secondary failure induced by a dynamic slip pulse. *Bulletin of the Seismological Society of America*, 95(1), 109–134. <https://doi.org/10.1785/0120030166>
- Roten, D., Olsen, K., & Day, S. (2017). Off-fault deformations and shallow slip deficit from dynamic rupture simulations with fault zone plasticity. *Geophysical Research Letters*, 44(15), 7733–7742. <https://doi.org/10.1002/2017gl074323>
- Savage, J., Burford, R., & Kinoshita, W. (1975). Earth movements from geodetic measurements. In G. Oakeshott (Ed.), *San Fernando earthquake of 9 February 1971* (Vol. 196, pp. 175–186). California Division of Mines and Geology.
- Savage, J., & Church, J. (1975). Evidence for afterslip on the San Fernando Fault. *Bulletin of the Seismological Society of America*, 65(4), 829–834. <https://doi.org/10.1785/bssa0650040829>
- Scott, C. P., Arrowsmith, J. R., Nissen, E., Lajoie, L., Maruyama, T., & Chiba, T. (2018). The M_7 2016 Kumamoto, Japan, earthquake: 3-D deformation along the fault and within the damage zone constrained from differential lidar topography. *Journal of Geophysical Research: Solid Earth*, 123(7), 6138–6155. <https://doi.org/10.1029/2018jb015581>
- Sharp, R. V. (1975). Displacement on tectonic ruptures. In G. Oakeshott (Ed.), *San Fernando earthquake of 9 February 1971* (Vol. 196, pp. 187–194). California Division of Mines and Geology.
- Stein, R. S., King, G. C., & Lin, J. (1994). Stress triggering of the 1994 $M = 6.7$ Northridge, California, earthquake by its predecessors. *Science*, 265(5177), 1432–1435. <https://doi.org/10.1126/science.265.5177.1432>
- Sylvester, A., & Pollard, D. (1975). Afterslip on the Sylmar fault segment. In G. Oakeshott (Ed.), *San Fernando earthquake of 9 February 1971* (Vol. 196, pp. 227–233). California Division of Mines and Geology.
- Templeton, E. L., & Rice, J. R. (2008). Off-fault plasticity and earthquake rupture dynamics: 1. Dry materials or neglect of fluid pressure changes. *Journal of Geophysical Research*, 113(B9), B09306. <https://doi.org/10.1029/2007jb005529>
- Thakur, P., & Huang, Y. (2021). Influence of fault zone maturity on fully dynamic earthquake cycles. *Geophysical Research Letters*, 48(17), e2021GL094679. <https://doi.org/10.1029/2021gl094679>
- Thakur, P., Huang, Y., & Kaneko, Y. (2020). Effects of low-velocity fault damage zones on long-term Earthquake behaviors on mature strike-slip faults. *Journal of Geophysical Research*, 125(8), e19587. <https://doi.org/10.1029/2020JB019587>

- Thomas, M. Y., & Bhat, H. S. (2018). Dynamic evolution of off-fault medium during an earthquake: A micromechanics based model. *Geophysical Journal International*, 214(2), 1267–1280. <https://doi.org/10.1093/gji/ggy129>
- Townley, S. D., & Allen, M. W. (1939). Descriptive catalog of earthquakes of the Pacific Coast of the United States 1769 to 1928. *Bulletin of the Seismological Society of America*, 29(1), 1–297. <https://doi.org/10.1785/bssa0290010001>
- Tsutsumi, H., & Yeats, R. S. (1999). Tectonic setting of the 1971 Sylmar and 1994 Northridge earthquakes in the San Fernando Valley, California. *Bulletin of the Seismological Society of America*, 89(5), 1232–1249. <https://doi.org/10.1785/bssa0890051232>
- Weber, F. H. (1975). Surface effects and related geology of the San Fernando earthquake in the Sylmar area. In G. Oakeshott (Ed.), *San Fernando earthquake of 9 February 1971* (Vol. 196, pp. 71–96). California Division of Mines and Geology.
- Wells, D. L., & Coppersmith, K. J. (1994). New empirical relationships among magnitude, rupture length, rupture width, rupture area, and surface displacement. *Bulletin of the Seismological Society of America*, 84(4), 974–1002.
- Wentworth, C. M., Yerkes, R., & Allen, C. R. (1971). Geologic setting and activity of faults in the San Fernando area, California. In *The San Fernando, California earthquake of February 9th* (pp. 6–16). U.S. Geological Survey Professional Paper 733.
- Wesnousky, S. G. (1988). Seismological and structural evolution of strike-slip faults. *Nature*, 335(6188), 340–343. <https://doi.org/10.1038/335340a0>
- Wesnousky, S. G. (1990). Seismicity as a function of cumulative geologic offset: Some observations from southern California. *Bulletin of the Seismological Society of America*, 80(5), 1374–1381.
- Wessell, P., Smith, W., Scharroo, R., Luis, J., & Wobbe, F. (2013). Generic Mapping Tools: Improved version released. *EOS Transactions*, 94(45), 409–410. <https://doi.org/10.1002/2013eo450001>
- Whitcomb, J. H., Allen, C. R., Garmany, J. D., & Hileman, J. A. (1973). San Fernando earthquake series, 1971: Focal mechanisms and tectonics. *Reviews of Geophysics*, 11(3), 693–730. <https://doi.org/10.1029/rg011i003p00693>
- Wollherr, S., Gabriel, A.-A., & Mai, P. M. (2019). Landers 1992 “reloaded”: Integrative dynamic earthquake rupture modeling. *Journal of Geophysical Research: Solid Earth*, 124(7), 6666–6702. <https://doi.org/10.1029/2018jb016355>
- Xu, X., Tong, X., Sandwell, D. T., Milliner, C. W., Dolan, J. F., Hollingsworth, J., et al. (2016). Refining the shallow slip deficit. *Geophysical Journal International*, 204(3), 1867–1886. <https://doi.org/10.1093/gji/ggv563>
- Yamashita, T. (2000). Generation of microcracks by dynamic shear rupture and its effects on rupture growth and elastic wave radiation. *Geophysical Journal International*, 143(2), 395–406. <https://doi.org/10.1046/j.1365-246x.2000.01238.x>
- Zielke, O., Galis, M., & Mai, P. M. (2017). Fault roughness and strength heterogeneity control earthquake size and stress drop. *Geophysical Research Letters*, 44(2), 777–783. <https://doi.org/10.1002/2016gl071700>
- Zinke, R., Dolan, J. F., Van Dissen, R., Grenader, J. R., Rhodes, E. J., McGuire, C. P., et al. (2015). Evolution and progressive geomorphic manifestation of surface faulting: A comparison of the Wairau and Awatere faults, South Island, New Zealand. *Geology*, 43(11), 1019–1022. <https://doi.org/10.1130/g37065.1>
- Zinke, R., Hollingsworth, J., & Dolan, J. F. (2014). Surface slip and off-fault deformation patterns in the 2013 M_w 7.7 Balochistan, Pakistan earthquake: Implications for controls on the distribution of near-surface coseismic slip. *Geochemistry, Geophysics, Geosystems*, 15(12), 5034–5050. <https://doi.org/10.1002/2014GC005538>
- Zinke, R., Hollingsworth, J., Dolan, J. F., & Van Dissen, R. (2019). Three-dimensional surface deformation in the 2016 M_w 7.8 Kaikōura, New Zealand, earthquake from optical image correlation: Implications for strain localization and long-term evolution of the Pacific–Australian plate boundary. *Geochemistry, Geophysics, Geosystems*, 20(3), 1609–1628. <https://doi.org/10.1029/2018GC007951>